Word Count: 5024

Ferroelastic post-stishovite transition mechanism revealed by single-crystal X-ray diffraction refinements at high pressure

YANYAO ZHANG[1,*], STELLA CHARITON[2], JIAMING HE[3], SUYU FU[1,4], VITALI B. PRAKAPENKA[2], JUNG-FU LIN[1,*]

[1]Department of Geological Sciences, Jackson School of Geosciences, The University of Texas at Austin, Austin, TX 78712, USA

[2]Center for Advanced Radiation Sources, The University of Chicago, IL 60637, USA

[3]Materials Science and Engineering Program, Mechanical Engineering, The University of Texas at Austin, Austin, Texas 78712, USA

[4]Present address: School of Earth and Space Exploration, Arizona State University, Tempe, AZ 85287, USA

*Corresponding authors: Yanyao Zhang (yanyaozhang@utexas.edu), Jung-Fu Lin (afu@jsg.utexas.edu)

ABSTRACT

The post-stishovite transition is a classic pseudo-proper typed ferroelastic transition with a symmetry-breaking spontaneous strain. This transition has been studied using high-pressure spontaneous strains, optic modes, and elastic moduli based on the Landau modeling, but its atomistic transformation mechanism remains unclear. Here we have conducted synchrotron single-crystal X-ray diffraction measurements on stishovite crystals up to 75.3 GPa in a

diamond-anvil cell. Analysis of data reveals atomic positions, bond lengths, bond angles, and variations of SiO_6 octahedra across the transition at high pressure. Our results show that the oxygen coordinates split at approximately 51.4 GPa where the apical and equatorial Si-O bond lengths cross over, the SiO_6 octahedral distortion vanishes, and the SiO_6 octahedra start to rotate about the *c* axis. These results are used to correlate with elastic moduli and Landau parameters in the symmetry-breaking strain e_1 - e_2 and order parameter Q to reveal the atomistic origin of the ferroelastic transition. When the bond lengths of two Si-O bonds are equal, the elastic modulus C_{11} converges with the C_{12} and the shear wave $V_{S1[110]}$ propagating along $[1\bar{1}0]$ and polarizing along [110] vanishes. The e_1 - e_2 and Q are proportional to the SiO_6 rotation angle. Our results on the pseudo-proper type transition are also compared with that for the proper-type in albite and improper-type in $CaSiO_3$ perovskite to shed new light on transition mechanisms in other types of the ferroelastic transitions. The symmetry-breaking strain in all these types of transitions arises as the primary effect from the structural angle, such as SiO_6 rotation or lattice constant angle, in the low-symmetry ferroelastic phase.

Keywords: single-crystal X-ray diffraction, stishovite, post-stishovite, ferroelastic transition, structural angle, Landau model, spontaneous strain

INTRODUCTION

Ferroelastic phase transitions occur in silicate minerals in the Earth's interior because of temperature and pressure perturbations. These transitions in crystals involve a change in point group with a symmetry-breaking strain (Aizu, 1969; Aizu, 1970). According to the Landau

theory, there are different types of the ferroelastic transitions, including proper, pseudo-proper, and improper types, which have different transition mechanisms (Carpenter and Salje, 1998; Wadhawan, 1982). The proper-type transition is driven by the symmetry-breaking spontaneous strain, whereas the pseudo-proper- and improper-type transitions are driven by other physical properties that are linearly and nonlinearly coupled to the symmetry-breaking strain, respectively (Carpenter et al., 1998; Wadhawan, 1982). These types of the ferroelastic phase transitions are also well known to be associated with elastic and optic mode anomalies including sound wave velocity softening, which could occur in some naturally abundant minerals under high pressure-temperature (P-T) conditions in the Earth's crust and mantle (Carpenter, 2006; Salje, 1990; Salje, 1992). Knowing their transition mechanisms and elastic properties in relevant P-T conditions can help us understand geophysics and geodynamics of the Earth's interior. For example, the proper-type ferroelastic transition in feldspar, comprising of approximately 41 wt% of the continental crust (Rudnick et al., 2003), has been linked to seismic low-velocity anomaly in the crust (Brown et al., 2006; Liu et al., 2018; Waeselmann et al., 2016; Zhang and Klemperer, 2005; Zhao et al., 2001). The stishovite and $CaSiO_3$ perovskite (CaPv) are abundant phases in the subducted mid-ocean ridge basalt (MORB) in the lower mantle (Ishii et al., 2019). Their transition mechanisms and elastic anomalies have been used to explain seismic heterogeneities, to infer the presence of the subducting slabs, and to constrain mantle convection at depths (Helffrich, 2006; Kaneshima, 2016; Niu et al., 2003; Sun et al., 2020; Thomson et al., 2019; Wang et al., 2020). As a prototype of six-fold coordinated silicates, the ferroelastic transition in stishovite is particularly important not only to aid our understanding in physical properties of subducting slabs in the mantle (Lakshtanov et al., 2007; Tsuchiya, 2011; Yang and Wu, 2014; Zhang et al., 2021), but also to

shed light on similar phase transitions in other rock-forming silicate and oxide minerals at depths.

The ferroelastic transition across the stishovite to post-stishovite phases at 50-55 GPa has been relatively well investigated using multiple experimental data sets including optical Raman modes, lattice constants from powder X-ray diffraction, and elastic moduli derived from sound velocities (Andrault et al., 2003; Buchen et al., 2018; Kingma et al., 1995; Lakshtanov et al., 2007; Zhang et al., 2021). These data are further complemented by Landau theory modeling (Carpenter et al., 2000; Hemley et al., 2000) and ab initio calculations (Karki et al., 1997a; Karki et al., 1997b; Yang and Wu, 2014). Importantly, experimental optic modes and lattice parameters across the transition have been used in the pseudo-proper type Landau modeling to show that the transition is driven by the soft B_{1g} mode and accompanied by a symmetry-breaking spontaneous strain and a significant shear softening (Andrault et al., 2003; Carpenter et al., 2000; Hemley et al., 2000; Kingma et al., 1995). A recent experimental study on elastic moduli (C_{ij}) of stishovite across the post-stishovite transition has further showed that the elastic modulus C_{11} converges with the C_{12} at the transition pressure, where the shear wave $V_{S1[110]}$ propagating along $[1\bar{1}0]$ and polarizing along [110] vanishes (Zhang et al., 2021). These results reveal macroscopic physical phenomena that need to be integrated with microscopic atomic displacements in order to have a complete understanding of the transition mechanism and physical properties. Along this line, crystal structural parameters, such as oxygen positions, bond lengths, and bond angles, are key to microscopically quantifying elastic anomalies and some Landau parameters such as the symmetry-breaking spontaneous strain. A previous powder X-ray diffraction (PXRD) study has refined crystal structures of stishovite and post-stishovite phases at high pressure using the Rietveld structural analysis method (Andrault et al., 1998). However, the refined structural

parameters showed considerable scattering at high pressure due to difficulties in solving crystal structures from the powder diffraction data (Harris et al., 2001). On the other hand, high-resolution single-crystal X-ray diffraction (SCXRD) studies on the stishovite are limited to 30 GPa, far below the transition pressure (Hill et al., 1983; Ross et al., 1990; Sinclair and Ringwood, 1978; Sugiyama et al., 1987; Yamanaka et al., 2002). This limitation was mainly due to the technical difficulty in conducting high-resolution SCXRD experiments at high pressure using a laboratory X-ray source. Recent advance in synchrotron X-ray diffraction technique now enables reliable crystal structure refinements to better understand the transition mechanism and elastic anomalies from the microscopic atomic perspective (Boffa Ballaran et al., 2013; Chariton et al., 2020; Clegg, 2019; Dera, 2010)

In this study, we performed synchrotron SCXRD experiments on stishovite crystals up to 75.3 GPa in a diamond anvil cell (DAC) with large X-ray opening equipped with Boehler-Almax anvils and seats. The crystal structure of the stishovite or post-stishovite phase has been solved and refined at each experimental pressure. Refined structural parameters show that the oxygen coordinates split at the transition pressure of ~51.4 GPa where the bond lengths of apical and equatorial Si-O bonds are equal. This atomic information is further used to evaluate deformation and rotation of the SiO_6 octahedron across the transition. Our results show that the distortion of the SiO_6 octahedron based on the Si-O bond lengths vanishes at the transition pressure where the SiO_6 octahedron starts to rotate about the *c* axis. Furthermore, we correlate the microscopic bond length difference of two Si-O bonds with the macroscopic elastic properties in the literature, such as elastic moduli C_{11} and C_{12} and acoustic velocity $V_{S1[110]}$ (Zhang et al., 2021). The symmetry-breaking spontaneous strain e_1 - e_2 and order parameter Q in the pseudo-proper type Landau model are quantified using the SiO_6 octahedral rotation angle Φ. The results show that the e_1 - e_2

and Q are proportional to the Φ. Finally, our results on the post-stishovite transition are applied to provide new insights into other types of the ferroelastic transitions in which the symmetry-breaking strain changes linearly with a given structural angle such as the SiO_6 rotation in $CaSiO_3$ perovskite or lattice constant angle in albite.

EXPERIMENTAL DETAILS

Stishovite single crystals were synthesized using a 1000-ton Kawai-type multi-anvil apparatus at the Institute for Planetary Materials, Okayama University (run# 1K1642). The synthesis and characterization of the crystals has been reported elsewhere (Xu et al., 2017; Zhang et al., 2021). Briefly, reagent-grade silicic acid of 99.9% purity (SiO_2 with 13 wt% H_2O) was used as the starting sample which was loaded into a platinum capsule. The sample assemblage was compressed to 12 GPa and then heated to 1873 K. The temperature of the assemblage was slowly cooled down to 1473 K where the sample was kept for 4 hours before quenched to ambient temperature and then decompressed to ambient pressure. Stishovite crystals recovered from the sample capsule are transparent and free of twinning domains and inclusions under optical and petrographic microscopes (Zhang et al., 2021). Electron microprobe analyses of a number of selected crystals show a chemical formula of SiO_2 without any other detectable elements. Analysis of unpolarized Fourier-transform infrared spectroscopic spectra shows ~19 ppm wt. water content in the selected crystals (Xu et al., 2017; Zhang et al., 2021). The amount of water in the Al-free stishovite crystals is consistent with previous reports (Litasov et al., 2007; Pawley et al., 1993).

Three stishovite crystals were loaded into a short-symmetric DAC with a pair of Boehler-Almax designed diamond anvils mounted onto WC seats with a large aperture of ~80º (4θ). This

allowed us to obtain reflections at a wide two theta range (2θ, Figure S1). The culet size of the diamond anvils is 200 μm in diameter. A rhenium gasket with an initial thickness of 260 μm was pre-indented to ~24 μm thick and subsequently a hole of 120 μm diameter was drilled in the center of the pre-indented area and used as the sample chamber. To obtain more reflections from stishovite, we selected three stishovite crystals with (2.4, 4.7, 1.7), (-0.8, 0.3, 1.6), and (0.8, 2.2, -0.9) orientations, respectively, which were determined by SCXRD measurements. The crystals were double-side polished down to approximately 7 μm thick using 3M diamond films. They were then cut into ~10-20 μm big platelets before being loaded into the sample chamber (Figure 1). Au powder (Goodfellow; 99.95% purity) was pressed into 2 μm thick, cut into ~5 μm wide disks, and placed close to the center of the sample chamber as the pressure calibrant (Fei et al., 2007). The three stishovite platelets were loaded at an equal distance to the Au calibrant to minimize possible pressure gradient across the crystals in the chamber (Figure 1c). Neon gas was loaded into the sample chamber as the pressure medium using a gas loading system at the Mineral Physics Laboratory of the University of Texas at Austin.

High-pressure SCXRD experiments were conducted up to 75.3 GPa at room temperature at 13ID-D beamline of the GSECARS, Advanced Photon Source, Argonne National Laboratory (Figures 1a and 1b). An incident X-ray beam of 0.2952 Å wavelength (42 keV energy) was focused down to a beam size of ~3×3 μm^2 at the sample position. Approximately 10% intensity of the incident X-ray was used for the measurements to avoid peak saturations. The sample stage was rotated over ±31º about the vertical axis of the DAC during data collections. The XRD patterns were collected using a CdTe Pilatus 1M detector with 1 or 2 s exposure time at every 0.5º step of the rotation. A membrane was used to increase and control pressure in the sample chamber. After each pressure increase, we monitored the pressure of the sample chamber until it

was stabilized before SCXRD measurements were conducted. Pressure uncertainties were evaluated from analysis of XRD spectra of Au collected right before and after each set of SCXRD measurements (Fei et al., 2007). Additionally, SCXRD measurements at ambient conditions were conducted in the Department of Chemistry at the University of Texas at Austin. A stishovite crystal with dimensions of approximately 0.94 × 0.44 × 0.17 mm was selected for the experiment. A SuperNova dual source diffractometer equipped with a Mo Kα radiation source (λ = 0.71073Å) and collimating mirror monochromators was used to collect XRD data. 2103 frames of data were collected using ω-scans with a scan range of 1º and a counting time of 1 s per frame.

The measured SCXRD data were used to solve the crystal structure and refine the atomic positions of the stishovite or post-stishovite phase at high pressure following a previous SCXRD processing method (Bykova, 2015). At a given pressure, we initialy used CrysAlis^{PRO} software to find unit cell, determine lattice parameters, extract intensity for each hkl reflection, and perform absorption corrections for each crystal (Rigaku, 2015). The reflection datasets from the three stishovite crystals were combined for the further analysis. JANA software was then used to determine the space group, resolve structure using a charge-flipping algorithm, and refine atomic coordinates and isotropic/anisotropic displacement parameters of the crystal (Petříček et al., 2014). On the other hand, the stishovite structure at ambient conditions was solved by direct methods and then refined together with anisotropic displacement parameters of Si and O atoms using SHELXL software (Sheldrick, 2015). Structural analysis of the Si and O atomic positions, bond lengths and bond angles was evaluated using the programs PLATON (Spek, 2009) and OLEX2 at ambient conditions (Dolomanov et al., 2009). The quality of the refinements at each pressure were

183 evaluated by residual *R*-factors such as R_{int} and R_1 (Bykova, 2015). The refined parameters of the
184 crystal structure were viewed and graphed using VESTA software (Momma and Izumi, 2011).
185
186 **RESULTS**
187 Analysis of the collected SCXRD images shows that reflection spots of the three crystals
188 display a round shape with a full-width at half maximum (FWHM) of less than 0.1º. The FWHM
189 is almost invariant up to 75.3 GPa, indicating that the single-crystal quality of stishovite was
190 preserved in compression in neon medium (Yamanaka et al., 2002) (Figures 1c and 1d). We
191 observed 66 to 239 total reflections from the crystals at high pressure (Figures 1a and 1b). These
192 reflections were then grouped into 31 to 55 unique reflections which were used to determine
193 lattice parameters at high pressure (Table 1). Furthermore, 24 to 63 reflections of $I > 3\sigma(I)$,
194 where I is the intensity and σ is the standard deviation, were used to determine the space group
195 and to refine atomic positions of the crystal at high pressure. Our analyses show that the crystal
196 is in the tetragonal stishovite structure with $P4_2/mnm$ (No. 136) space group at pressures up to
197 49.8 GPa (Figures S2 and S3; Tables 1 and S1). From 52.4 GPa to 75.3 GPa, the crystal is stable
198 in an orthorhombic structure with *Pnnm* (No. 58) space group, called the $CaCl_2$-type post-
199 stishovite phase (Figures S2 and S3; Tables 1 and S1). These results indicate that the post-
200 stishovite phase transition occurs between 49.8 and 52.4 GPa, consistent with previous studies
201 (Andrault et al., 1998; Hemley et al., 2000; Kingma et al., 1995; Zhang et al., 2021). The R_{int} and
202 R_1 values are 0.6-14.9% and 1.3-9.4%, respectively, indicating the refined crystal structures are
203 of good quality (Table 1).
204 Atomic coordinates, bond lengths, and bond angles can be derived from the refined crystal
205 structures (Figures 2 and 3; Table 2). Using Si atom positions in the stishovite structure as the

reference, the x (or y) coordinate of oxygen relative to the Si positions only changes from 0.306 at ambient conditions to 0.303 at 49.8 GPa (Figures 2a and 3a). That is, the O atoms remain almost stationary. Crossing into the post-stishovite phase, the x coordinate of oxygen drastically decreases from 0.303 at 52.4 GPa to 0.279 at 75.3 GPa whereas the y coordinate drastically increases from 0.303 to 0.323 (Figure 3a). This splitting of oxygen coordinates corresponds to a splitting of a- and b-axis in the post-stishovite phase (Figure S2a). On the other hand, the Si-O bond lengths decrease continuously with increasing pressure up to 75.3 GPa (Figures 2 and 3b). The apical Si-O3 bond length is initially much longer than the equatorial Si-O1(2) bond length at ambient conditions, but it decreases with increasing pressure much faster than the equatorial Si-O1(2) bond length. This anisotropic linear incompressibility behavior leads to an equal bond length of 1.703 Å for the two Si-O bonds at ~51.4 GPa where the post-stishovite transition occurs (Figures 3b). In the post-stishovite structure, the apical Si-O3 bond becomes shorter than the equatorial Si-O1(2) bond (Figures 2b and 3b). Additionally, the bond angles between Si and O atoms in the stishovite structure are almost unaffected by increasing pressure up to ~51 GPa: ∠O1(2)-Si-O3 = 90º, ∠O1-Si-O2 = ~81.3º, and ∠O1(2)-Si-O1(2) = ~98.7º (Figure 3c). Crossing into the post-stishovite phase, the bond angles are slightly changed: ∠O1-Si-O2 increases by 0.5º, ∠O1(2)-Si-O1(2) decreases by 0.5º, and ∠O1-Si-O3 or ∠O2-Si-O3 remains almost unchanged within uncertainties (~0.1º) up to 75.3 GPa. Accordingly, the O1-O2 interatomic distance remains unchanged under compression whereas the O1(2)-O1(2), O1-O3, and O2-O3 distances decrease with increasing pressure and the difference between O1-O3 and O2-O3 distance is negligible (Figure S4).

The aforementioned structural parameters are used to further analyze the volume, deformation, and rotation of the SiO_6 octahedron across the post-stishovite transition (Figures 2 and 4; Table

3). These analyses show that the SiO_6 volume decreases continuously with increasing pressure up to 75.3 GPa, resulting in a continuous decrease of the unit-cell volume (Figures S2b and S5). The deformation of SiO_6 octahedron can be quantitatively determined by the distortion index and the bond angle variance based on the refined bond lengths and bond angles, respectively. The distortion index is defined as $D\ (\%) = \frac{100}{6}\sum_{n=1}^{6}|l_i - l_{av}|/l_{av}$ where the l_i is the Si-O bond length and the l_{av} is the average Si-O bond length (Renner and Lehmann, 1986). The bond angle variance is defined as $\sigma^2(\mathrm{deg}^2) = \frac{1}{11}\sum_{i=1}^{12}(\alpha_i - 90°)^2$ where the α_i is the O-Si-O bond angle (Robinson et al., 1971). In the stishovite phase, the distortion index decreases from 1.3% at ambient pressure to zero at ~51.4 GPa whereas the bond angle variance remains invariant at approximately 27 deg^2 with increasing pressure up to ~51.4 GPa (Figures 4a and 4b). Crossing into the post-stishovite phase, the distortion index increases to approximately 0.3% whereas the bond angle variance decreases to approximately 24 deg^2 at ~75 GPa (Figures 4a and 4b). On the other hand, the rotation of the SiO_6 octahedron about the *c* axis can be evaluated with respect to the stishovite structure using a formula, $\Phi\ (°) = 45° - \arctan(ax_O/by_O)$, where the y_O and x_O are *y*- and *x*-coordinate of oxygen atoms, respectively (Bärnighausen et al., 1984; Range et al., 1987) (Figure 4c). These analyses show that the SiO_6 octahedron does not rotate in the stishovite phase but starts to rotate about the *c* axis crossing into the post-stishovite phase. At 75.3 GPa, the SiO_6 octahedral rotation is about 5.4º.

Our structural refinement results for stishovite are, for the first order, consistent with previous SCXRD studies up to 30 GPa (Hill et al., 1983; Ross et al., 1990; Sinclair and Ringwood, 1978; Sugiyama et al., 1987; Yamanaka et al., 2002) (Figures 3 and 4). Additionally, our results across the post-stishovite transition are generally consistent with a PXRD study using the Rietveld structural analysis (Andrault et al., 1998), except for the octahedral volume (Figure S5). We note

that our SCXRD data have much higher resolutions and are denser in the vicinity of the transition pressure such that detailed structural evolutions are clearly revealed across the post-stishovite transition. On the other hand, comparisons between ab initio calculations and experimental results show very large discrepancies in the structural parameters especially for the post-stishovite phase (Figures 3 and 4). For example, theoretical calculations show equal equatorial and apical Si-O bond lengths in the post-stishovite structure at high pressure (Karki et al., 1997b), which is contrary to our results. This could be due to difficulties in properly optimizing spontaneous strains in the post-stishovite phase to account for exchange-correlation interactions in the local-density approximation (LDA). This in turn can affect accuracy in theoretically-predicted elastic moduli across the ferroelastic post-stishovite transition which are quite different from experimentally-derived elastic moduli (Karki et al., 1997a; Yang and Wu, 2014; Zhang et al., 2021). Our study here not only provides reliable structural models of the stishovite and post-stishovite phases, but also serves as benchmarks for future ab initio calculations.

DISCUSSION

Our single-crystal X-ray diffraction refinements on the refined Si and O coordinates, Si-O bond lengths, and O-Si-O bond angles across the post-stishovite transition can be used to correlate with previous elasticity and Landau modeling studies to shed new light on the pseudo-proper type ferroelastic transition (Carpenter et al., 2000; Hemley et al., 2000; Zhang et al., 2021). The elastic modulus C_{11} increases with decreasing Si-O bond length difference but flattens when the difference is below 0.01 Å, while the C_{12} increases significantly across the transition (Figure 5a). As a result, the elastic modulus $(C_{11} - C_{12})/2$, which reflects the strain

response to the shear stress along the [110] direction in the stishovite structure (Bell and Rupprecht, 1963), becomes zero when the apical and equatorial Si-O bond lengths become equal and the distortion of the SiO_6 octahedron vanishes (Figures 3b and 4a). Accordingly, the $C_{11} - C_{12}$, one of Born criteria of the tetragonal stishovite phase, becomes zero at the phase transition (Zhang et al., 2021). Crossing into the post-stishovite phase, the C_{11} splits into the C_{11} and C_{22} as the oxygen coordinates split (Figures 3a and 5a). As the bond length of the equatorial Si-O1(2) bond becomes longer than that of the apical Si-O3 bond, the C_{11}, C_{22}, and C_{12} moduli of the post-stishovite phase increase (Figure 5a). The corresponding Born criterion, $C_{11}C_{22} - C_{12}^2$, becomes positive in the post-stishovite phase, indicating its stability after the crossover of the equatorial Si-O1(2) and apical Si-O3 bond lengths. On the other hand, the ferroelastic post-stishovite transition is also manifested by vanishing shear wave $V_{S1[110]}$ (Zhang et al., 2021). The $V_{S1[110]}$ decreases from 5.5 km/s to zero as the Si-O bond length difference decreases from 0.05 Å to zero (Figure 5b). Across into the post-stishovite phase, the $V_{S1[110]}$ increases as the Si-O bond length difference increases.

We also use the structural parameters to quantify the spontaneous strains (e_1 and e_2) and order parameter Q in Landau modeling of the pseudo-proper type ferroelastic transition at high pressure (Figure 6). The splitting of oxygen coordinates leads to a symmetry reduction from the tetragonal stishovite to the orthorhombic post-stishovite structure. Because the $y_O > x_O$ in the orthorhombic post-stishovite phase (Figure 3a), the *a* axis becomes shorter whereas the *b* axis becomes longer with respect to the stishovite lattice structure (Figure 6a). All these lead to the occurrence of a negative spontaneous strain e_1 and a positive spontaneous strain e_2 (Figure 6a). Additionally, as oxygen atom coordinates deviate from the diagonal direction of the *ab* plane (Figures 2 and 3a), the SiO_6 octahedron rotates about the *c* axis in the post-stishovite structure

(Figure 6a). Our results further show that the symmetry-breaking strain e_1 - e_2, whose eigenvalue is the aforementioned elastic modulus $C_{11} - C_{12}$, can be quantified by the SiO_6 rotation angle Φ (Figure 6b). That is, the e_1 - e_2 is proportional to the Φ angle. Because the order parameter Q is coupled linearly to the e_1 - e_2 strain, the Q also changes linearly with the Φ angle (Figure 6c).

These crystallographic results can be correlated with Landau modeling parameters to have a better understanding of the transition. Previous studies have shown that the post-stishovite transition belongs to the pseudo-proper type which is driven by the soft B_{1g} optic mode (Carpenter et al., 2000; Kingma et al., 1995). The Raman active B_{1g} mode represents an anticlockwise rotational vibration of oxygen atoms about the *c* axis (Hemley et al., 1986; Traylor et al., 1971). As the two Si-O bond lengths cross over each other (Figure 3b), the Raman shifts of the B_{1g} optic mode decrease and would become zero at the critical pressure (P_C = 110.2 GPa) (Kingma et al., 1995; Zhang et al., 2021). However, the transition occurs at a much lower pressure of ~51.4 GPa where the two Si-O bond lengths are equal (Figure 3b). The oxygen coordinates split across the transition (Figure 3a), leading to a symmetry breaking from the point group 422 to 222 where one 4-fold axis becomes a 2-fold axis. This symmetry reduction further results in the rotation of the SiO_6 octahedra about the *c* axis and the appearance of spontaneous strains. The eigenvalue $C_{11} - C_{12}$ and acoustic $V_{S1[110]}$ accordingly vanish at the transition, leading to significant shear wave velocity softening (Zhang et al., 2021). Therefore, the Si-O bond lengths and SiO_6 octahedra rotation play a key role in the ferroelastic transition from the stishovite to the post-stishovite phase.

IMPLICATIONS

As discussed in the introduction, pseudo-proper, proper and improper typed ferroelastic transitions can occur in representative naturally-occurring silicate minerals in Earth's deep crust and mantle. The ferroelastic transitions are manifested by appearance of the symmetry-breaking spontaneous strain in the low-symmetry ferroelastic phase (Wadhawan, 1982). Although the driving force is different among these ferroelastic transitions, their symmetry-breaking strains all couple linearly or nonlinearly to the order parameter (Carpenter and Salje, 1998). Our study on the post-stishovite transition, a typical pseudo-proper typed ferroelastic transition, reveals the relationship between the macroscopic spontaneous strain and microscopic structural angle (Figure 7a). Correlation between the symmetry-breaking strains and microscopic structural parameters in these ferroelastic transitions can thus provide additional information to better understand their transition mechanisms and elastic anomalies. Along this line, we have evaluated these parameters in proper and improper typed ferroelastic transitions and compare the results with our post-stishovite transition data.

Proper typed ferroelastic transition occurs in albite ($NaAlSi_3O_8$ feldspar) from monoclinic (space group: $C2/m$) to triclinic (space group: $C\bar{1}$) structure at approximately 1300 K (Salje, 1985; Salje et al., 1985). Albite is an abundant silicate in Earth's deep crust so knowing the transition mechanism can have implications in understanding physical properties of the region (Mookherjee et al., 2016; Salje, 1992; Smith and Brown, 1988; Zhang and Klemperer, 2005). The spontaneous shear strain is directly related to the order parameter (i.e., $e_4 \propto Q$) (Salje, 1985; Salje et al., 1985). Microscopically, the transition is induced by the collapse of the crankshafts around large Na cations in the lattice structure (Hayward and Salje, 1996). Therefore, the spontaneous strain e_4 should be related to the degree of such collapse which can be measured using lattice constant angle α between a and b axis; that is, $e_4 \propto$ -cos α (Carpenter et al., 1998;

Kroll et al., 1980). Using experimental data from early reports (Hayward and Salje, 1996; Kroll et al., 1980), the strain e_4 is found to increase linearly with the |cos α| in the triclinic ferroelastic phase (Figure 7b). Since it is a proper-type transition (Carpenter and Salje, 1998), the order parameter Q emerges and changes linearly with the |cos α| in the triclinic structure. As a consequence, the corresponding shear modulus C_{44} is expected to drop to zero at the phase transition (Carpenter et al., 1998).

Improper typed ferroelastic transition occurs in CaPv from cubic to tetragonal phase at approximately 450 K and 12 GPa with a nearly flat phase boundary in the P-T phase diagram (Kurashina et al., 2004; Sun et al., 2016). The CaPv has been recently discovered as inclusions in diamond which was named davemaoite (Tschauner et al., 2021). The CaPv is also believed to comprise of approximately 20 vol% subducted MORB materials in the upper part of the lower mantle (Ishii et al., 2019). Because the CaPv structure consists of SiO_6 units, similar to the stishovite structure, the transition is also manifested by the tilting and/or rotation of the SiO_6 octahedra (Carpenter et al., 2001). Here, we quantify the symmetry-breaking strain (e_{Pv}) with the rotation angle of the SiO_6 octahedron about the c axis (Φ_{Pv}) (Figure 7c). The e_{Pv} and Φ_{Pv} can be evaluated by the formula, $e_{Pv} = \sqrt{2/3}(c-a)/a_0$ and $\Phi_{Pv} = cos^{-1}\left(\sqrt{2}a/c\right)$, respectively, where the a and c are lattice parameters of the tetragonal phase and the a_0 is the extrapolated lattice parameter of the cubic phase (Zhao et al., 1993a; Zhao et al., 1993b). Analysis of high-temperature lattice parameters at approximately 12 GPa by Thomson et al. (2019) shows that the SiO_6 octahedron rotates about the c axis below ~450 K in the tetragonal phase but does not rotate between 450 and 1400 K in the cubic structure (Figure 7c). Importantly, the e_{Pv} is proportional to the Φ_{Pv}^2 in the tetragonal phase. Because the Φ_{Pv} is also the order parameter across the cubic-tetragonal transition, the spontaneous strain has a nonlinear coupling with the order parameter,

reflecting the nature of the improper-type ferroelastic transition (Wadhawan, 1982). Furthermore, the eigenvalue $C_{11} - C_{12}$ is expected to behave abnormally across the transition (Carpenter and Salje, 1998). This is consistent with recent experimental results showing reductions in sound wave velocity across the transition, which may affect seismic wave properties of subducting slabs in the lower mantle (Gréaux et al., 2019; Sun et al., 2020; Thomson et al., 2019).

We have examined three types of ferroelastic transitions using representative silicate minerals in the Earth's crust and mantle. Depending on the transition mechanisms, a given structural angle, such as the lattice constant angle or octahedral rotation angle, can be used to correlate with the symmetry-breaking spontaneous strain. The ferroelastic transitions are displacive second-order transitions (Carpenter, 2006; Salje et al., 2005). Thus, a slight change in the structural angle cannot abruptly change the first derivative of the free energy (the "second-order" feature), but it is sufficient to remove at least one symmetric element in the lattice structure (a change of the point group) across the transition. This symmetry reduction must instantaneously induce the spontaneous strains in the low-symmetry phase compared to the high-symmetry structure (Carpenter et al., 1998). Our results further reveal that the symmetry-breaking strain changes linearly with a given structural angle in all types of the transitions. This means that the symmetry-breaking strain occurs as the primary effect from the structural angle in the low-symmetry ferroelastic phase. Therefore, the change of structural angle is the atomistic origin of the ferroelastic transition with a symmetry-breaking spontaneous strain. Our results here can be combined with sound velocity studies across the three types of ferroelastic transitions in silicates and oxides at high pressure. This helps shed light on the abnormal seismic properties across the transitions especially in the subducting slabs and deep crustal regions.

ACKNOWLEDGEMENTS

We thank Fang Xu for her assistances on the synthesis and characterization of the single-crystal stishovite. We also thank Vincent Lynch for his assistance on SCXRD measurements at ambient conditions and data analysis. High-pressure SCXRD experiments were performed at 13ID-D, GSECARS.

FUNDING

GSECARS was supported by the National Science Foundation (EAR-0622171) and U.S. Department of Energy (DE-FG0294ER14466) under contract DE-AC0206CH11357. Jung-Fu Lin acknowledges support from Geophysics Program of the U.S. National Science Foundation (EAR-1916941 and EAR-2001381) and the Joint-Use User Program of the Institute for Planetary Materials, Okayama University.

REFERENCES CITED

Aizu, K. (1969) Possible species of “ferroelastic” crystals and of simultaneously ferroelectric and ferroelastic crystals. Journal of the Physical society of Japan, 27(2), 387-396.

-. (1970) Determination of the state parameters and formulation of spontaneous strain for ferroelastics. Journal of the Physical Society of Japan, 28(3), 706-716.

Andrault, D., Angel, R.J., Mosenfelder, J.L., and Bihan, T.L. (2003) Equation of state of stishovite to lower mantle pressures. American Mineralogist, 88(2-3), 301-307.

Andrault, D., Fiquet, G., Guyot, F., and Hanfland, M. (1998) Pressure-induced Landau-type transition in stishovite. Science, 282(5389), 720-724.

Bärnighausen, H., Bossert, W., and Anselment, B. (1984) A second-order phase transition of calcium bromide and its geometrical interpretation. Acta Crystallographica Section A, 40.

Bell, R., and Rupprecht, G. (1963) Elastic constants of strontium titanate. Physical Review, 129(1), 90.

Birch, F. (1947) Finite elastic strain of cubic crystals. Physical review, 71(11), 809.

Boffa Ballaran, T., Kurnosov, A., and Trots, D. (2013) Single-crystal X-ray diffraction at extreme conditions: a review. High Pressure Research, 33(3), 453-465.

Brown, J., Abramson, E., and Angel, R. (2006) Triclinic elastic constants for low albite. Physics and Chemistry of Minerals, 33(4), 256-265.

Buchen, J., Marquardt, H., Schulze, K., Speziale, S., Boffa Ballaran, T., Nishiyama, N., and Hanfland, M. (2018) Equation of State of Polycrystalline Stishovite Across the Tetragonal-Orthorhombic Phase Transition. Journal of Geophysical Research: Solid Earth, 123(9), 7347-7360.

Bykova, E. (2015) Single-crystal X-ray diffraction at extreme conditions in mineral physics and material sciences.

Carpenter, M.A. (2006) Elastic properties of minerals and the influence of phase transitions. American mineralogist, 91(2-3), 229-246.

Carpenter, M.A., Becerro, A.I., and Seifert, F. (2001) Strain analysis of phase transitions in (Ca, Sr) TiO3 perovskites. American Mineralogist, 86(3), 348-363.

Carpenter, M.A., Hemley, R.J., and Mao, H.k. (2000) High-pressure elasticity of stishovite and the P42/mnm⇌ Pnnm phase transition. Journal of Geophysical Research: Solid Earth, 105(B5), 10807-10816.

Carpenter, M.A., and Salje, E.K. (1998) Elastic anomalies in minerals due to structural phase transitions. European Journal of Mineralogy, 693-812.

Carpenter, M.A., Salje, E.K., and Graeme-Barber, A. (1998) Spontaneous strain as a determinant of thermodynamic properties for phase transitions in minerals. European Journal of Mineralogy, 621-691.

Chariton, S., Bykov, M., Bykova, E., Koemets, E., Fedotenko, T., Winkler, B., Hanfland, M., Prakapenka, V.B., Greenberg, E., and McCammon, C. (2020) The crystal structures of Fe-bearing MgCO3 sp2- and sp3-carbonates at 98 GPa from single-crystal X-ray diffraction using synchrotron radiation. Acta Crystallographica Section E: Crystallographic Communications, 76(5), 715-719.

Clegg, W. (2019) The development and exploitation of synchrotron single-crystal diffraction for chemistry and materials. Philosophical Transactions of the Royal Society A, 377(2147), 20180239.

Dera, P. (2010) All different flavors of synchrotron single crystal X-ray diffraction experiments. High-pressure crystallography, p. 11-22. Springer.

Dolomanov, O.V., Bourhis, L.J., Gildea, R.J., Howard, J.A., and Puschmann, H. (2009) OLEX2: a complete structure solution, refinement and analysis program. Journal of applied crystallography, 42(2), 339-341.

Fei, Y., Ricolleau, A., Frank, M., Mibe, K., Shen, G., and Prakapenka, V. (2007) Toward an internally consistent pressure scale. Proceedings of the National Academy of Sciences, 104(22), 9182-9186.

Gréaux, S., Irifune, T., Higo, Y., Tange, Y., Arimoto, T., Liu, Z., and Yamada, A. (2019) Sound velocity of CaSiO 3 perovskite suggests the presence of basaltic crust in the Earth's lower mantle. Nature, 565(7738), 218.

Harris, K.D., Tremayne, M., and Kariuki, B.M. (2001) Contemporary advances in the use of powder X-ray diffraction for structure determination. Angewandte Chemie International Edition, 40(9), 1626-1651.

Hayward, S.A., and Salje, E.K. (1996) Displacive phase transition in anorthoclase; the "plateau effect" and the effect of T1-T2 ordering on the transition temperature. American Mineralogist, 81(11-12), 1332-1336.

Helffrich, G. (2006) Small-scale seismic heterogeneity and mantle structure. Astronomy & Geophysics, 47(1), 1.20-1.26.

Hemley, R., Mao, H.-K., and Chao, E. (1986) Raman spectrum of natural and synthetic stishovite. Physics and chemistry of Minerals, 13(5), 285-290.

Hemley, R., Shu, J., Carpenter, M., Hu, J., Mao, H., and Kingma, K. (2000) Strain/order parameter coupling in the ferroelastic transition in dense SiO2. Solid State Communications, 114(10), 527-532.

Hill, R., Newton, M., and Gibbs, G. (1983) A crystal chemical study of stishovite. Journal of Solid State Chemistry, 47(2), 185-200.
Ishii, T., Kojitani, H., and Akaogi, M. (2019) Phase Relations of Harzburgite and MORB up to the Uppermost Lower Mantle Conditions: Precise Comparison With Pyrolite by Multisample Cell High-Pressure Experiments With Implication to Dynamics of Subducted Slabs. Journal of Geophysical Research: Solid Earth.
Kaneshima, S. (2016) Seismic scatterers in the mid-lower mantle. Physics of the Earth and Planetary Interiors, 257, 105-114.
Karki, B.B., Stixrude, L., and Crain, J. (1997a) Ab initio elasticity of three high-pressure polymorphs of silica. Geophysical Research Letters, 24(24), 3269-3272.
Karki, B.B., Warren, M., Stixrude, L., Ackland, G., and Crain, J. (1997b) Ab initio studies of high-pressure structural transformations in silica. Physical Review B, 55(6), 3465.
Kingma, K.J., Cohen, R.E., Hemley, R.J., and Mao, H.-k. (1995) Transformation of stishovite to a denser phase at lower-mantle pressures. Nature, 374(6519), 243.
Kroll, H., Bambauer, H.U., and Schirmer, U. (1980) The high albite–monalbite and analbite–monalbite transitions. American Mineralogist, 65(11-12), 1192-1211.
Kurashina, T., Hirose, K., Ono, S., Sata, N., and Ohishi, Y. (2004) Phase transition in Al-bearing CaSiO3 perovskite: implications for seismic discontinuities in the lower mantle. Physics of the Earth and Planetary Interiors, 145(1-4), 67-74.
Lakshtanov, D.L., Sinogeikin, S.V., Litasov, K.D., Prakapenka, V.B., Hellwig, H., Wang, J., Sanches-Valle, C., Perrillat, J.-P., Chen, B., and Somayazulu, M. (2007) The post-stishovite phase transition in hydrous alumina-bearing SiO2 in the lower mantle of the earth. Proceedings of the National Academy of Sciences, 104(34), 13588-13590.
Litasov, K.D., Kagi, H., Shatskiy, A., Ohtani, E., Lakshtanov, D.L., Bass, J.D., and Ito, E. (2007) High hydrogen solubility in Al-rich stishovite and water transport in the lower mantle. Earth and Planetary Science Letters, 262(3), 620-634.
Liu, W., Yang, Y., Xia, Q., Ye, Y., Wang, Z., Zhang, P., and Li, G. (2018) Water decreases displacive phase transition temperature in alkali feldspar. European Journal of Mineralogy, 30(6), 1071-1081.
Momma, K., and Izumi, F. (2011) VESTA 3 for three-dimensional visualization of crystal, volumetric and morphology data. Journal of applied crystallography, 44(6), 1272-1276.
Mookherjee, M., Mainprice, D., Maheshwari, K., Heinonen, O., Patel, D., and Hariharan, A. (2016) Pressure induced elastic softening in framework aluminosilicate-albite (NaAlSi 3 O 8). Scientific reports, 6(1), 1-10.
Niu, F., Kawakatsu, H., and Fukao, Y. (2003) Seismic evidence for a chemical heterogeneity in the midmantle: A strong and slightly dipping seismic reflector beneath the Mariana subduction zone. Journal of Geophysical Research: Solid Earth, 108(B9).
Pawley, A.R., McMillan, P.F., and Holloway, J.R. (1993) Hydrogen in stishovite, with implications for mantle water content. SCIENCE-NEW YORK THEN WASHINGTON-, 261, 1024-1024.
Petříček, V., Dušek, M., and Palatinus, L. (2014) Crystallographic computing system JANA2006: general features. Zeitschrift für Kristallographie-Crystalline Materials, 229(5), 345-352.
Range, K.-J., Rau, F., Klement, U., and Heyns, A. (1987) β-PtO2: high pressure synthesis of single crystals and structure refinement. Materials research bulletin, 22(11), 1541-1547.
Renner, B., and Lehmann, G. (1986) Correlation of angular and bond length distortions in TO4 units in crystals. Zeitschrift für Kristallographie-Crystalline Materials, 175(1-2), 43-59.
Rigaku, O. (2015) Crysalis Pro. Rigaku Oxford Diffraction, Yarnton, England.
Robinson, K., Gibbs, G., and Ribbe, P. (1971) Quadratic elongation: a quantitative measure of distortion in coordination polyhedra. Science, 172(3983), 567-570.

514 Ross, N.L., Shu, J., and Hazen, R.M. (1990) High-pressure crystal chemistry of stishovite. American
515 Mineralogist, 75(7-8), 739-747.
516 Rudnick, R., Gao, S., Holland, H., and Turekian, K. (2003) Composition of the continental crust. The crust,
517 3, 1-64.
518 Salje, E. (1985) Thermodynamics of sodium feldspar I: order parameter treatment and strain induced
519 coupling effects. Physics and Chemistry of Minerals, 12(2), 93-98.
520 -. (1990) Phase transitions in ferroelastic and co-elastic crystals. Ferroelectrics, 104(1), 111-120.
521 Salje, E., Kuscholke, B., Wruck, B., and Kroll, H. (1985) Thermodynamics of sodium feldspar II:
522 experimental results and numerical calculations. Physics and Chemistry of Minerals, 12(2), 99-
523 107.
524 Salje, E.K. (1992) Application of Landau theory for the analysis of phase transitions in minerals. Physics
525 reports, 215(2), 49-99.
526 Salje, E.K., Hayward, S.A., and Lee, W.T. (2005) Ferroelastic phase transitions: structure and
527 microstructure. Acta Crystallographica Section A: Foundations of Crystallography, 61(1), 3-18.
528 Sheldrick, G.M. (2015) Crystal structure refinement with SHELXL. Acta Crystallographica Section C:
529 Structural Chemistry, 71(1), 3-8.
530 Sinclair, W., and Ringwood, A. (1978) Single crystal analysis of the structure of stishovite. Nature,
531 272(5655), 714.
532 Smith, J., and Brown, W. (1988) Feldspar minerals, Crystal structures, physical, chemical and
533 microtextural properties, Springer. Berlin Heidelberg New York, 828.
534 Spek, A.L. (2009) Structure validation in chemical crystallography. Acta Crystallographica Section D:
535 Biological Crystallography, 65(2), 148-155.
536 Sugiyama, M., Endo, S., and Koto, K. (1987) The crystal structure of stishovite under pressure up to 6
537 GPa. Mineralogical Journal, 13(7), 455-466.
538 Sun, N., Bian, H., Zhang, Y., Lin, J.-F., Prakapenka, V.B., and Mao, Z. (2020) High-Pressure Experimental
539 Study of Tetragonal CaSiO 3-Pervoskite to 200 GPa. AGU Fall Meeting Abstracts, 2020, p.
540 MR016-0011.
541 Sun, N., Mao, Z., Yan, S., Wu, X., Prakapenka, V.B., and Lin, J.F. (2016) Confirming a pyrolitic lower
542 mantle using self-consistent pressure scales and new constraints on CaSiO3 perovskite. Journal
543 of Geophysical Research: Solid Earth, 121(7), 4876-4894.
544 Thomson, A., Crichton, W., Brodholt, J., Wood, I., Siersch, N., Muir, J., Dobson, D., and Hunt, S. (2019)
545 Seismic velocities of CaSiO 3 perovskite can explain LLSVPs in Earth's lower mantle. Nature,
546 572(7771), 643-647.
547 Traylor, J.G., Smith, H., Nicklow, R., and Wilkinson, M. (1971) Lattice dynamics of rutile. Physical Review
548 B, 3(10), 3457.
549 Tschauner, O., Huang, S., Yang, S., Humayun, M., Liu, W., Gilbert Corder, S.N., Bechtel, H.A., Tischler, J.,
550 and Rossman, G.R. (2021) Discovery of davemaoite, CaSiO3-perovskite, as a mineral from the
551 lower mantle. Science, 374(6569), 891-894.
552 Tsuchiya, T. (2011) Elasticity of subducted basaltic crust at the lower mantle pressures: Insights on the
553 nature of deep mantle heterogeneity. Physics of the Earth and Planetary Interiors, 188(3-4),
554 142-149.
555 Wadhawan, V.K. (1982) Ferroelasticity and related properties of crystals. Phase Transitions: A
556 Multinational Journal, 3(1), 3-103.
557 Waeselmann, N., Brown, J.M., Angel, R.J., Ross, N., Zhao, J., and Kaminsky, W. (2016) The elastic tensor
558 of monoclinic alkali feldspars. American Mineralogist, 101(5), 1228-1231.
559 Wang, W., Xu, Y., Sun, D., Ni, S., Wentzcovitch, R., and Wu, Z. (2020) Velocity and density characteristics
560 of subducted oceanic crust and the origin of lower-mantle heterogeneities. Nature
561 Communications, 11(1), 1-8.

Xu, F., Yamazaki, D., Sakamoto, N., Sun, W., Fei, H., and Yurimoto, H. (2017) Silicon and oxygen self-diffusion in stishovite: Implications for stability of SiO2-rich seismic reflectors in the mid-mantle. Earth and Planetary Science Letters, 459, 332-339.

Yamanaka, T., Fukuda, T., and Mimaki, J. (2002) Bonding character of SiO 2 stishovite under high pressures up to 30 GPa. Physics and Chemistry of Minerals, 29(9), 633-641.

Yang, R., and Wu, Z. (2014) Elastic properties of stishovite and the CaCl 2-type silica at the mantle temperature and pressure: An ab initio investigation. Earth and Planetary Science Letters, 404, 14-21.

Zhang, Y., Fu, S., Wang, B., and Lin, J.-F. (2021) Elasticity of a Pseudoproper Ferroelastic Transition from Stishovite to Post-Stishovite at High Pressure. Physical Review Letters, 126(2), 025701.

Zhang, Z., and Klemperer, S.L. (2005) West-east variation in crustal thickness in northern Lhasa block, central Tibet, from deep seismic sounding data. Journal of Geophysical Research: Solid Earth, 110(B9).

Zhao, W., Mechie, J., Brown, L., Guo, J., Haines, S., Hearn, T., Klemperer, S., Ma, Y., Meissner, R., and Nelson, K. (2001) Crustal structure of central Tibet as derived from project INDEPTH wide-angle seismic data. Geophysical Journal International, 145(2), 486-498.

Zhao, Y., Weidner, D.J., Parise, J.B., and Cox, D.E. (1993a) Critical phenomena and phase transition of perovskite—data for NaMgF3 perovskite. Part II. Physics of the Earth and Planetary Interiors, 76(1-2), 17-34.

-. (1993b) Thermal expansion and structural distortion of perovskite—data for NaMgF3 perovskite. Part I. Physics of the Earth and Planetary Interiors, 76(1-2), 1-16.

FIGURE 1. Representative single-crystal X-ray diffraction data of stishovite and post-stishovite at high pressure. (a) and (b) show original diffraction images at 28.5 GPa for stishovite and at 75.3 GPa for post-stishovite, respectively. Sample reflection spots are marked with red open circles. (c) An optical image of the sample chamber showing three crystals (P1, P2, and P3) and gold pressure calibrant (Au) in neon pressure medium (Ne) at 2.8 GPa. (d) Full-width at half maximum (FWHM) of a selected 101 diffraction peak as a function of pressure. The FWHM of the peak (red solid circles) remains almost unchanged during compression. The insert panel shows a round 101 reflection spot and its integrated peak with FWHM of 0.07º at 75.3 GPa. These data indicate that the single crystal quality was preserved in compression up to 75.3 GPa.

FIGURE 2. Representative refined crystal structures of stishovite and post-stishovite at high pressure. (a) Stishovite at 49.8 GPa; (b) post-stishovite at 73.8 GPa. Silicon (Si) and oxygen (O1, O2, and O3) atoms are shown as blue and red balls, respectively. Lattice parameters, Si-O bond lengths, and O1-Si-O1 bond angles are labelled in the representative structures, and can also be found in Tables 1 and S1. Black arrows in (b) show Φ rotation angle of 5.1º which is the SiO_6 octahedron rotation about the *c* axis with respect to the ideal stishovite structure in (a).

FIGURE 3. Oxygen coordinates, Si-O bond lengths, and O-Si-O bond angles across the post-stishovite transition at high pressure. (a) Oxygen coordinates as a function of pressure. The *x* and *y* coordinates for oxygen are almost invariant in stishovite; however, *x* coordinate decreases and *y* coordinate increases with increasing pressure in the post-stishovite phase. (b) Si-O bond lengths as a function of pressure. The bond length in the apical Si-O3 and in the equatorial Si-O1(2) becomes equivalent to each other within uncertainties at the post-stishovite transition. (c) O-Si-O bond angles as a function of pressure. The angles remain almost constant in the stishovite phase, while ∠O1-Si-O2 increases and ∠O1(2)-Si-O1(2) decreases with increasing pressure in the post-stishovite phase. Please refer to Figure 2 for the meaning of the oxygen atom numbering. Solid lines in (b) show the best fits using an axial incompressibility equation of state (Birch, 1947), while those in (a) and (c) are the best polynomial fits to guide the eyes. Note that the data and fit for ∠O1-Si-O3 are drawn in green in order to distinguish it from ∠O2-Si-O3. The gray vertical band shows the phase transition region at ~51.4 GPa based on the splitting of the oxygen coordinates. Literature single-crystal and powder XRD and ab initio data are plotted

for comparison (Andrault et al., 1998; Hill et al., 1983; Karki et al., 1997b; Ross et al., 1990; Sinclair and Ringwood, 1978; Sugiyama et al., 1987; Yamanaka et al., 2002).

FIGURE 4. Refined SiO_6 octahedron parameters of stishovite and post-stishovite at high pressure. (a) Bond length distortion (D) of the octahedron as a function of pressure. The distortion vanishes at the transition. (b) Angle variance (σ^2) of the octahedron as a function of pressure. It remains constant in stishovite but decreases with increasing pressure in the post-stishovite phase. (c) The rotation of the SiO_6 octahedron about the c axis (Φ) with pressure only occurs in the post-stishovite phase (also see Figure 2 for the rotation). Lines show the best polynomial fits to the data. The gray vertical band represents the transition pressure. Previous studies are also shown for comparison (Andrault et al., 1998; Hill et al., 1983; Karki et al., 1997b; Ross et al., 1990; Sinclair and Ringwood, 1978; Sugiyama et al., 1987; Yamanaka et al., 2002).

FIGURE 5. Elastic moduli and shear wave velocity of stishovite and post-stishovite as a function of the bond length difference between the apical and equatorial Si-O bonds. (a) Selected elastic moduli, C_{11}, C_{12}, and C_{22}; (b) transverse shear wave $V_{S1[110]}$ polarizing along $[1\bar{1}0]$ and propagating along [110] direction. Elasticity data are taken from Zhang et al. (2021). Bond length data from this study are shown in the solid circles with both red and green colors for figure clarity. When the apical bond length is equal to the equatorial bond length, the C_{11} converges with C_{12} in (a) and the $V_{S1[110]}$ vanishes in (b). The gray vertical band shows the post-stishovite phase transition region. Early studies are also plotted for comparison (Andrault et al., 1998; Hill et al., 1983; Karki et al., 1997b; Ross et al., 1990; Sinclair and Ringwood, 1978; Sugiyama et al., 1987; Yamanaka et al., 2002).

FIGURE 6. Landau parameters as a function of the SiO_6 rotation angle Φ about the c axis across the post-stishovite transition. (a) Schematics to highlight the rotation of the SiO_6 octahedron and the occurrence of the spontaneous strains e_1 and e_2 in (b). Blue and red spheres represent Si and O atoms, respectively. The ab plane of the post-stishovite unit cell is schematically drawn in the pink area with dashed lines, whereas the aa plane in the stishovite structure is shown in the blue area with solid lines for comparison for the lattice rotation. (b) Symmetry-breaking spontaneous

strain (e_1 - e_2) and (c) order parameter Q as a function of the Φ angle. Crossing into the post-stishovite phase, the (e_1 - e_2) and Q emerge and increase linearly with the Φ in (a) and (b), respectively. The gray vertical band shows the transition pressure. Literature data are plotted for comparison (Andrault et al., 1998; Hill et al., 1983; Ross et al., 1990; Sinclair and Ringwood, 1978; Sugiyama et al., 1987; Yamanaka et al., 2002).

FIGURE 7. Symmetry-breaking spontaneous strains as a function of angle parameters in three different types of ferroelastic transitions in representative rock-forming silicate minerals. (a) The $|e_1 - e_2|$ as a function of the Φ angle across the pseudo-proper type post-stishovite transition in this study. (b) The strain e_4 as a function of the |cos α| across the proper-type monoclinic-triclinic transition in the albite, where the α is the lattice angle between the a and b axis. Red circles: Hayward and Salje (1996); green circles: Kroll et al. (1980). (c) The e_{Pv}×50 as a function of squared SiO_6 rotation angle about the c axis, Φ_{Pv}^2, across the improper-type cubic-tetragonal transition in the $CaSiO_3$ perovskite (CaPv). Experimental data from Thomson et al. (2019) were used for the analysis. The lines in (a)-(c) are the best linear fits to the data. The gray vertical bands show the transition region.

TABLE 1. Structure refinement results for the stishovite and post-stishovite at high pressure

P, GPa	space group	a, Å	b, Å	c, Å	V, Å^3	unique refl[1]	R_{int}, %	R_1, %
0	$P4_2/mnm$	4.1752(1)		2.6642(1)	46.443(3)	2788	4.63	1.29
2.8(1)	$P4_2/mnm$	4.1660(3)		2.6640(3)	46.24(1)	55	0.61	3.48
7.8(1)	$P4_2/mnm$	4.1416(5)		2.6564(3)	45.57(1)	48	1.52	5.93
13.0(2)	$P4_2/mnm$	4.1200(4)		2.6458(3)	44.91(1)	37	0.78	6.28
16.0(1)	$P4_2/mnm$	4.1066(4)		2.6433(4)	44.58(1)	50	5.89	6.14
16.9(3)	$P4_2/mnm$	4.1045(4)		2.6393(3)	44.464(8)	48	0.35	6.11
19.7(1)	$P4_2/mnm$	4.0891(4)		2.6298(17)	43.97(3)	50	1.65	3.78
21.4(1)	$P4_2/mnm$	4.0875(4)		2.6366(3)	44.05(1)	41	12.74	6.00
26.8(2)	$P4_2/mnm$	4.0681(5)		2.6259(5)	43.46(1)	43	4.37	7.84
28.5(2)	$P4_2/mnm$	4.0520(4)		2.6162(18)	42.95(3)	52	1.70	7.73
33.8(2)	$P4_2/mnm$	4.0318(6)		2.6070(8)	42.38(2)	48	5.80	6.17
40.4(2)	$P4_2/mnm$	4.0133(7)		2.6000(30)	41.88(5)	34	8.91	5.61
48.7(2)	$P4_2/mnm$	3.9875(7)		2.5840(30)	41.09(5)	46	1.06	5.65
49.8(2)	$P4_2/mnm$	3.9819(10)		2.5810(60)	40.92(10)	36	1.01	5.35
52.4(2)	$Pnnm$	3.9440(30)	4.0150(19)	2.5851(13)	40.93(4)	47	1.25	5.66
54.2(2)	$Pnnm$	3.9320(30)	4.0128(18)	2.5817(12)	40.73(4)	56	0.87	5.38
55.6(2)	$Pnnm$	3.9300(40)	4.0097(10)	2.5750(5)	40.58(4)	54	4.82	6.22
58.6(3)	$Pnnm$	3.9140(50)	4.0118(12)	2.5717(6)	40.38(5)	31	14.89	4.97
62.0(3)	$Pnnm$	3.9010(40)	4.0089(12)	2.5656(8)	40.12(4)	41	2.94	6.88
64.4(3)	$Pnnm$	3.8880(40)	4.0080(20)	2.5681(14)	40.01(5)	46	4.80	6.66
65.8(3)	$Pnnm$	3.8820(40)	4.0070(10)	2.5667(8)	39.93(4)	41	12.90	6.62
68.0(3)	$Pnnm$	3.8710(40)	4.0051(10)	2.5616(7)	39.71(4)	41	1.40	6.85
71.0(3)	$Pnnm$	3.8580(30)	4.0040(9)	2.5580(7)	39.51(3)	46	1.91	4.57
73.8(3)	$Pnnm$	3.8500(30)	4.0016(8)	2.5557(6)	39.37(3)	45	2.60	6.05
75.3(3)	$Pnnm$	3.8380(20)	3.9974(7)	2.5498(5)	39.12(2)	46	0.55	4.42

[1]unique refl: number of unique observed reflections

TABLE 2. Oxygen positions, bond lengths, and bond angles of the stishovite and post-stishovite at high pressure. Please refer to Fig. 2 for the meaning of the atom symbols.

P,GPa	oxygen position		bond length, Å		bond angle, º			
	x	y	Si-O3	Si-O1(2)	∠O1-Si-O3	∠O2-Si-O3	∠O1(2)-Si-O1(2)	∠O1-Si-O2
0	0.3061(1)	0.3061(1)	1.8075(6)	1.7565(4)	90.00(5)	90.00(5)	98.65(5)	81.35(5)
2.8(1)	0.3060(3)	0.3060(3)	1.803(1)	1.755(1)	90.00(7)	90.00(7)	98.74(7)	81.26(7)
7.8(1)	0.3052(5)	0.3052(5)	1.788(3)	1.751(1)	90.00(9)	90.00(9)	98.67(8)	81.33(8)
13.0(2)	0.3046(5)	0.3046(5)	1.775(3)	1.745(1)	90.00(9)	90.00(9)	98.57(8)	81.43(8)
16.0(1)	0.3046(5)	0.3046(5)	1.769(3)	1.742(1)	90.00(9)	90.00(9)	98.70(8)	81.30(8)
16.9(3)	0.3046(3)	0.3046(3)	1.7681(13)	1.7401(9)	90.00(9)	90.00(9)	98.64(8)	81.36(8)
19.7(1)	0.3039(5)	0.3039(5)	1.757(3)	1.736(2)	90.00(9)	90.00(9)	98.45(8)	81.55(8)
21.4(1)	0.3044(6)	0.3044(6)	1.760(3)	1.737(2)	90.00(10)	90.00(10)	98.76(9)	81.24(9)
26.8(2)	0.3048(6)	0.3048(6)	1.754(3)	1.728(2)	90.00(10)	90.00(10)	98.92(9)	81.08(9)
28.5(2)	0.3038(6)	0.3038(6)	1.741(3)	1.725(2)	90.00(10)	90.00(10)	98.64(9)	81.36(9)
33.8(2)	0.3036(4)	0.3036(4)	1.731(2)	1.719(1)	90.00(8)	90.00(8)	98.67(8)	81.33(8)
40.4(2)	0.3036(4)	0.3036(4)	1.7231(17)	1.7125(16)	90.00(10)	90.00(10)	98.78(9)	81.22(9)
48.7(2)	0.3028(5)	0.3028(5)	1.708(3)	1.705(2)	90.00(9)	90.00(9)	98.56(8)	81.44(8)
49.8(2)	0.3023(4)	0.3023(4)	1.702(2)	1.704(3)	90.00(8)	90.00(8)	98.43(8)	81.57(8)
52.4(2)	0.2943(12)	0.3106(5)	1.704(4)	1.705(3)	89.87(15)	90.13(15)	98.59(14)	81.41(14)
54.2(2)	0.2912(12)	0.3121(5)	1.697(4)	1.706(3)	89.92(15)	90.08(15)	98.38(14)	81.62(14)
55.6(2)	0.2927(7)	0.3127(6)	1.702(3)	1.6986(18)	89.91(12)	90.09(12)	98.57(11)	81.43(11)
58.6(3)	0.2877(12)	0.3152(6)	1.693(4)	1.701(3)	89.96(14)	90.04(14)	98.21(13)	81.79(13)
62.0(3)	0.2854(16)	0.3167(8)	1.689(5)	1.699(4)	89.98(16)	90.02(16)	98.06(15)	81.94(15)
64.4(3)	0.2850(14)	0.3175(7)	1.687(5)	1.698(4)	89.91(16)	90.09(16)	98.28(15)	81.72(15)
65.8(3)	0.2841(14)	0.3188(7)	1.688(5)	1.696(3)	89.94(15)	90.06(15)	98.34(15)	81.66(15)
68.0(3)	0.2814(12)	0.3200(6)	1.682(4)	1.696(3)	89.96(14)	90.04(14)	98.09(14)	81.91(14)
71.0(3)	0.2807(9)	0.3211(5)	1.681(3)	1.693(2)	89.90(12)	90.10(12)	98.17(12)	81.83(12)
73.8(3)	0.2794(12)	0.3216(6)	1.677(4)	1.692(3)	89.90(14)	90.10(14)	98.07(14)	81.93(14)
75.3(3)	0.2788(8)	0.3231(4)	1.677(3)	1.687(2)	89.90(11)	90.10(11)	98.17(11)	81.83(11)

730 **TABLE 3.** Volume (V_{oct}), bond length distortion (D), angle variance (σ^2), and rotation angle
731 about c axis (Φ) of the SiO_6 octahedron in the stishovite and post-stishovite at high pressure

P,GPa	V_{oct}, Å^3	D	σ^2, deg^2	Φ, º
0	7.351(2)	0.01278(3)	27.186(7)	0
2.8(1)	7.319(4)	0.01196(7)	27.75(2)	0
7.8(1)	7.224(8)	0.00923(10)	27.35(3)	0
13.0(2)	7.128(8)	0.00745(8)	26.70(3)	0
16.0(1)	7.075(8)	0.00685(8)	27.52(3)	0
16.9(3)	7.057(9)	0.00711(11)	27.16(3)	0
19.7(1)	6.988(8)	0.00537(6)	25.96(3)	0
21.4(1)	6.994(9)	0.00582(7)	27.92(3)	0
26.8(2)	6.895(8)	0.00662(8)	28.91(3)	0
28.5(2)	6.828(9)	0.00412(5)	27.16(3)	0
33.8(2)	6.738(5)	0.00325(3)	27.32(2)	0
40.4(2)	6.659(5)	0.00276(2)	28.01(2)	0
48.7(2)	6.542(8)	0.00075(1)	26.66(3)	0
49.8(2)	6.522(10)	0.00053(1)	25.85(4)	0
52.4(2)	6.530(13)	0.00036(4)	26.85(5)	2.1(2)
54.2(2)	6.511(13)	0.00225(1)	25.52(5)	2.6(2)
55.6(2)	6.473(8)	0.00076(1)	26.71(3)	2.5(1)
58.6(3)	6.466(13)	0.00204(4)	24.52(5)	3.3(2)
62.0(3)	6.435(16)	0.00270(7)	23.63(6)	3.8(2)
64.4(3)	6.418(18)	0.00274(11)	24.92(7)	4.0(2)
65.8(3)	6.405(14)	0.00221(5)	25.31(5)	4.2(2)
68.0(3)	6.386(13)	0.00366(7)	23.79(5)	4.6(2)
71.0(3)	6.356(9)	0.00304(4)	24.26(3)	4.9(1)
73.8(3)	6.341(13)	0.00396(8)	23.68(5)	5.1(2)
75.3(3)	6.300(8)	0.00259(3)	24.29(3)	5.4(1)

732

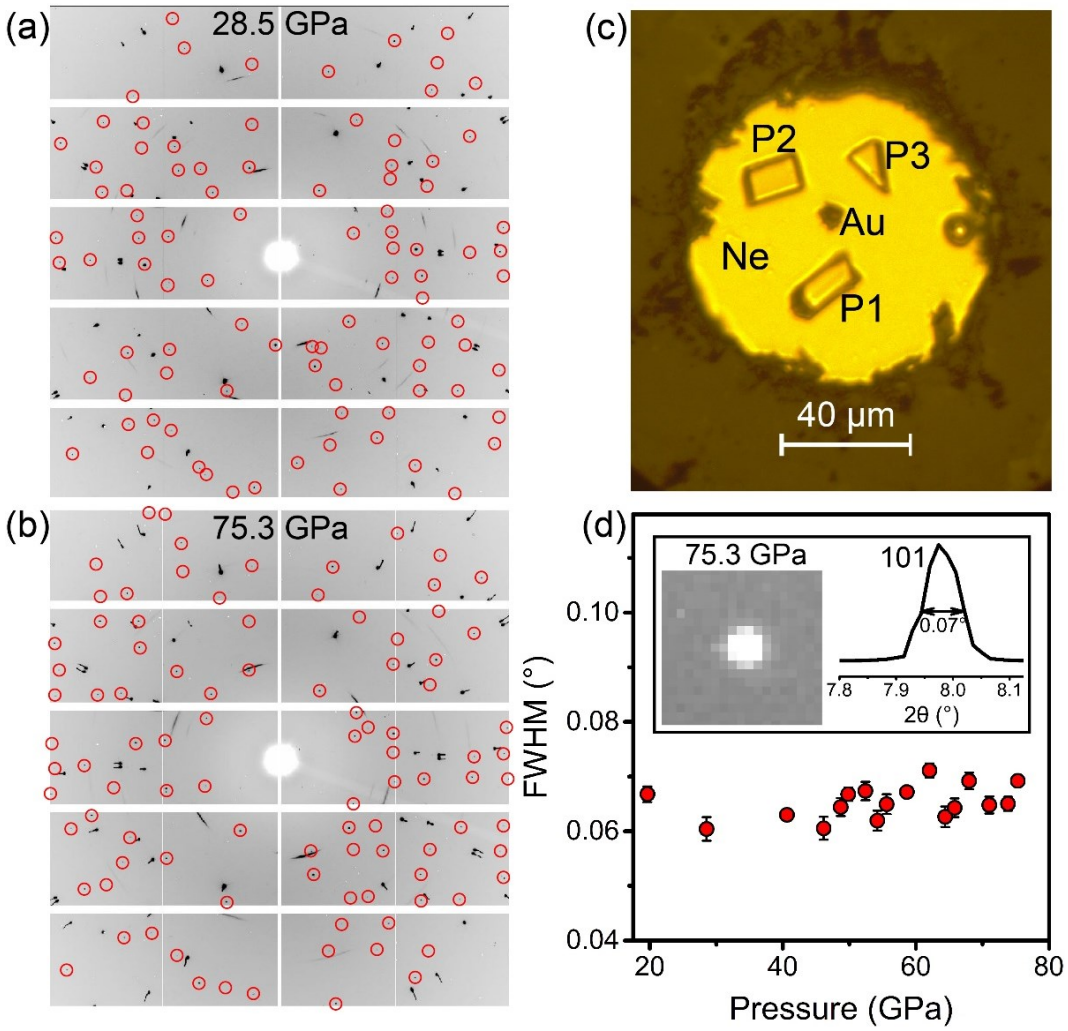

733

734

735

736

737

738

739

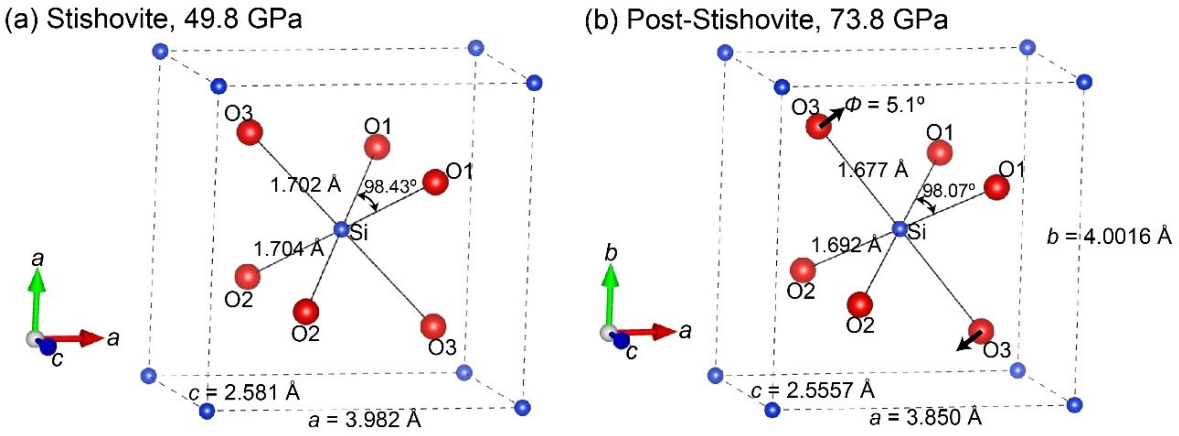
(a) Stishovite, 49.8 GPa
O3
O1
O1
1.702 Å
98.43°
Si
1.704 Å
O2
O2
O3
a
a
c
c = 2.581 Å
a = 3.982 Å
(b) Post-Stishovite, 73.8 GPa
O3
Φ = 5.1°
O1
1.677 Å
O1
98.07°
Si
1.692 Å
b = 4.0016 Å
O2
O2
O3
b
a
c
c = 2.5557 Å
a = 3.850 Å

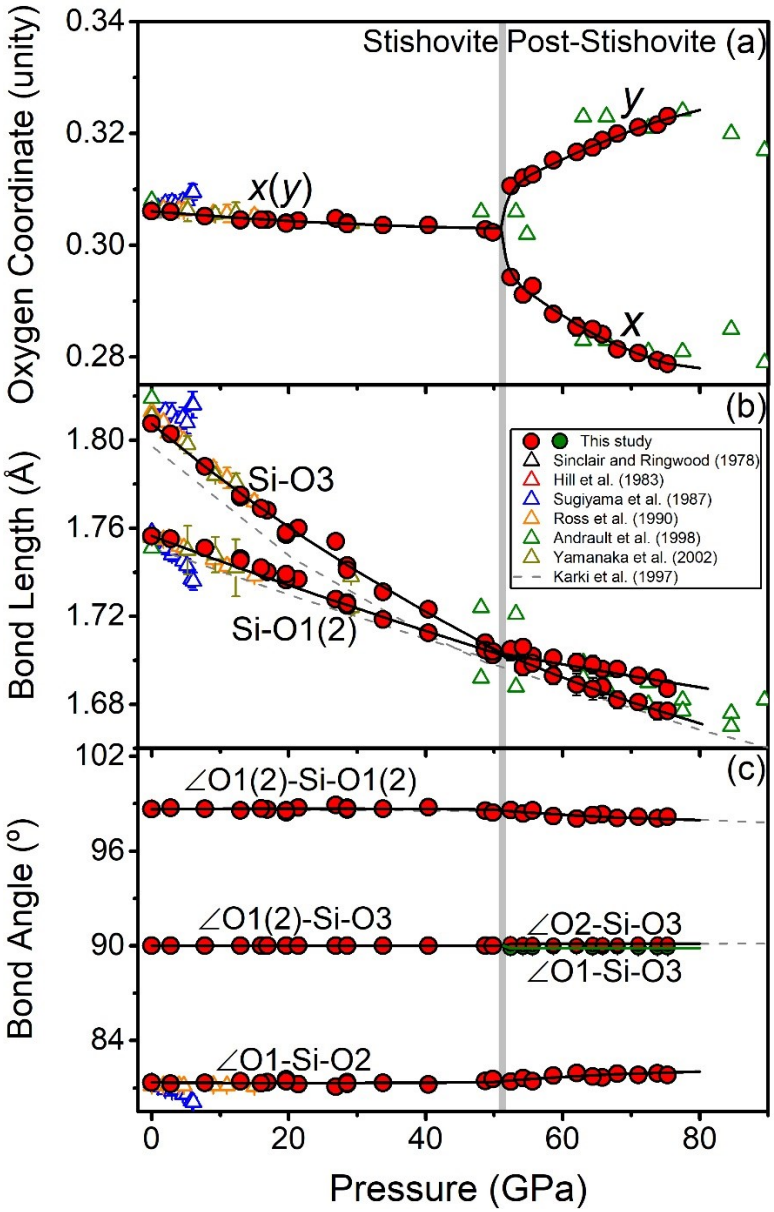

750

751

752

753

754

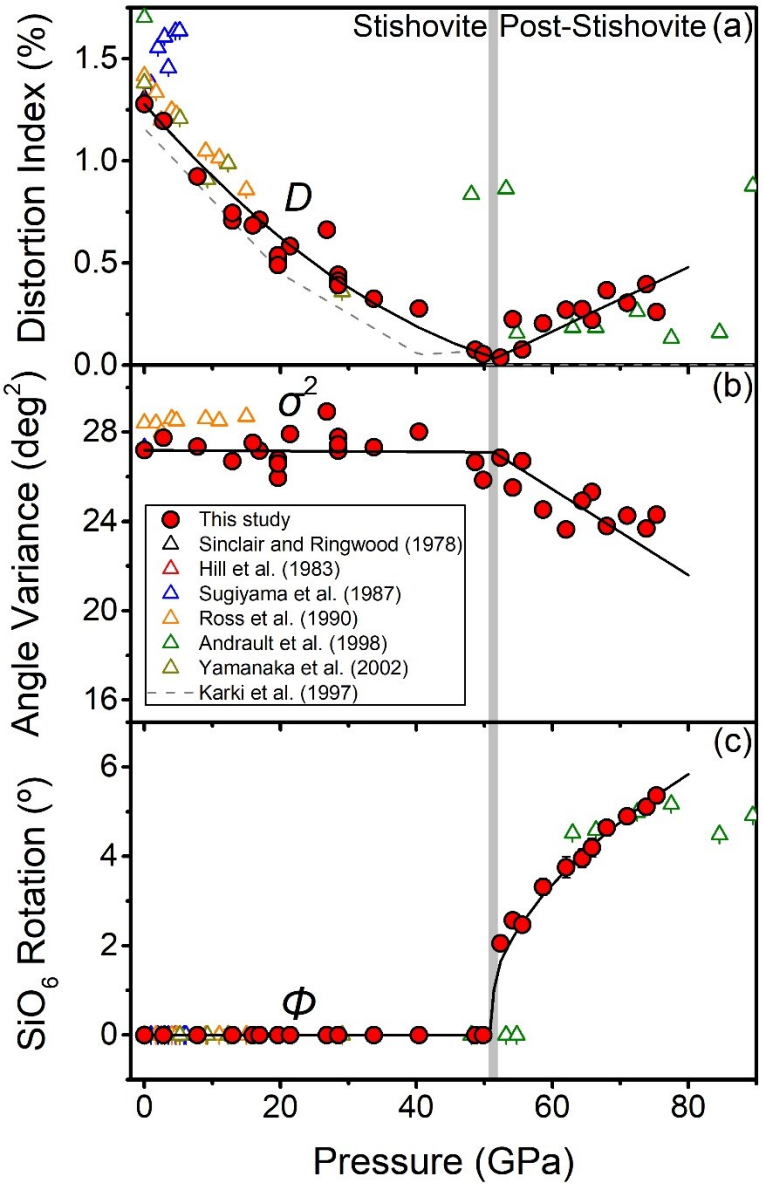
Stishovite
Post-Stishovite
(a)
(b)
(c)
D
σ²
Φ
Distortion Index (%)
Angle Variance (deg²)
SiO6 Rotation (°)
Pressure (GPa)
This study
Sinclair and Ringwood (1978)
Hill et al. (1983)
Sugiyama et al. (1987)
Ross et al. (1990)
Andrault et al. (1998)
Yamanaka et al. (2002)
Karki et al. (1997)

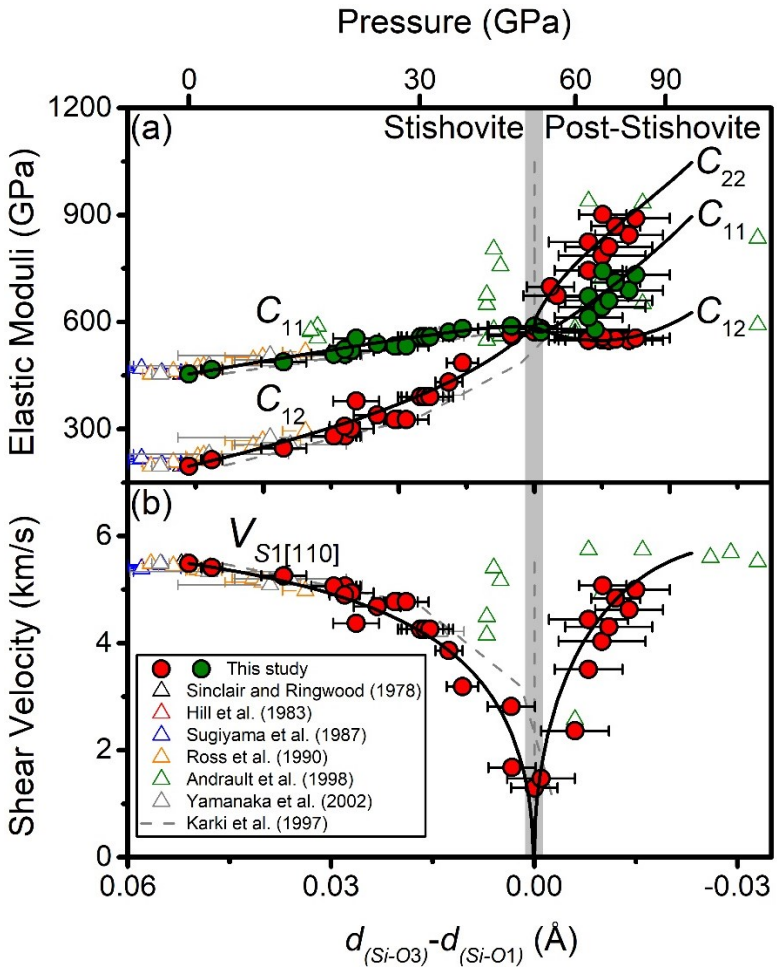

763

764

765

766

767

768

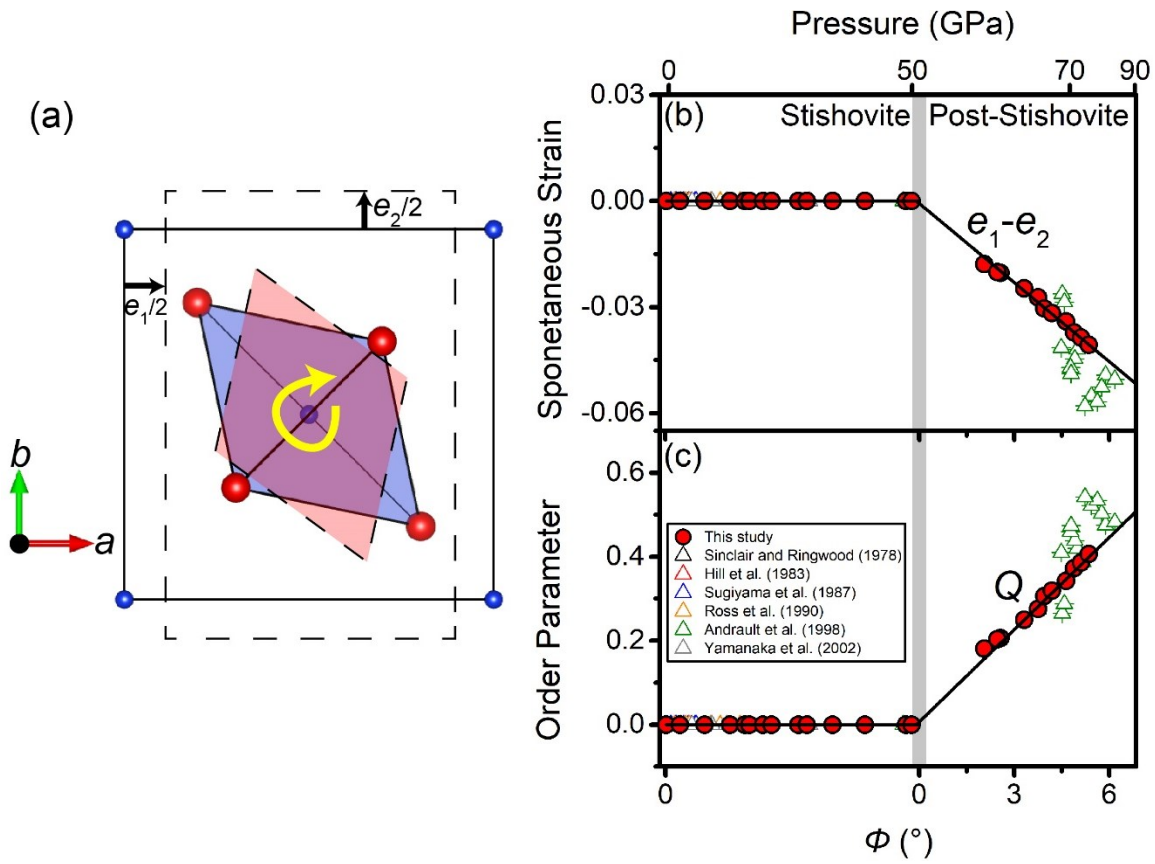
(a)
$e_2/2$
$e_1/2$
b
a
Pressure (GPa)
0
50
70
90
(b)
Stishovite
Post-Stishovite
0.03
0.00
-0.03
-0.06
Sponetaneous Strain
e_1-e_2
(c)
0.6
0.4
0.2
0.0
Order Parameter
Q
This study
Sinclair and Ringwood (1978)
Hill et al. (1983)
Sugiyama et al. (1987)
Ross et al. (1990)
Andrault et al. (1998)
Yamanaka et al. (2002)
0
0
3
6
Φ (°)

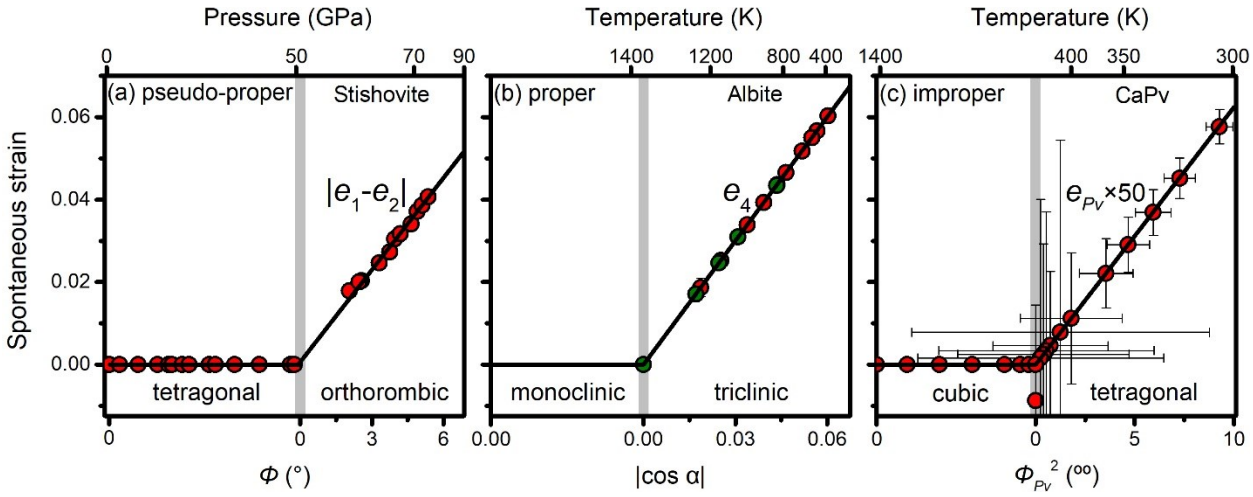
Pressure (GPa)
Temperature (K)
Temperature (K)
Spontaneous strain
(a) pseudo-proper
Stishovite
$|e_1-e_2|$
tetragonal
orthorombic
Φ (°)
(b) proper
Albite
e_4
monoclinic
triclinic
|cos α|
(c) improper
CaPv
e_{Pv}×50
cubic
tetragonal
Φ_{Pv}^2 (°°)

783